IoT-Driven Regression Tree Models for Efficient Microwave Dielectric Material Characterization: Addressing Non-Linear Cavity Sensing

Ahmad Khusro, Zubair Akhter, *Member, IEEE*, Abhishek K. Jha, *Senior Member, IEEE*, Atif Shamim, *Fellow, IEEE*, and Mohammad S. Hashmi, *Senior Member, IEEE*

***Abstract*—Interconnected microwave dielectric sensing nodes have the potential to revolutionize microwave material processing and design, where microwave dielectric materials characterization (MDMC) with high precision and rapid circuit design are crucial. This research presents an Internet of Things (IoT)-enabled automated MDMC system designed to tackle the nonlinearity challenges in the extended cavity perturbation regime. Utilizing a cylindrical cavity operating in TE_{111} mode at 5 GHz, the proposed MDMC system is extensively trained on a diverse range of materials through numerous full-wave 3-D electromagnetic simulations. The outputs, i.e., relative permittivity and loss tangent, are derived using advanced machine learning models, including decision tree (DT) and ensemble learning (EL). A comparative analysis that incorporates simulation, measurement, and predicted permittivity values across varying sample dimensions demonstrates the robustness and accuracy of the DT and EL model. This validates the effectiveness of our high-quality sensor node and sophisticated data processing techniques within an IoT-centric framework.**

***Index Terms*—Complex permittivity, dielectric properties, machine learning (ML), microwave material characterization, microwave material industry, microwave resonant sensing, regression tree model, smart industry.**

I. Introduction

ACCURATE identification and characterization of dielectric materials are vital to effectively design and optimize microwave components, including filters, antennas, and sensors [1], [2], [3], [4]. In the development cycle of microwave component design, the ability to obtain precise estimates of the dielectric properties of substrate materials beforehand can significantly enhance overall development efficiency by reducing the number of design iterations. With the rapid evolution of 5G technologies, the reliable characterization of sub-6 GHz frequencies is essential for effectively targeting 5G frequency bands [5], [6]. Over the past few decades, microwave dielectric characterization has been an active research area, generally divided into two main categories: resonant [7], [8], [9], [10], [11], [12] and nonresonant [13], [14], [15], [16], [17], [18], [19], [20]. While resonant cavity perturbation is typically viewed as a more accurate technique for dielectric characterization of materials, it encounters significant challenges. Specifically, when the ratio of the sample volume (V_s) to the cavity volume (V_c) exceeds 0.005 [8], this method faces substantial limitations due to nonlinearity. Although existing models have provided valuable insights for accurately characterizing dielectric samples, they struggle to estimate permittivity (ε_r') and loss tangent ($\tan\delta$) in these extended nonlinear regions, leading to considerable deviations ($>20\%$) from actual measured values. This article utilizes a resonant circular cavity as an Internet of Things (IoT) sensing node, augmented by an artificial intelligence (AI) algorithm to ensure precise estimation of ε_r' and $\tan\delta$ even in these nonlinear regimes.

AI and machine learning (ML) have become important tools in radio frequency (RF)/Microwave engineering, with applications in areas, such as sensing [21], antenna design [22], [23], device modeling [24], [25], [26], characterization of dielectric sheets [14], [15], [31], and RF circuit design [27], [28], [29]. Various ML techniques, including artificial neural networks (ANNs), support vector regression (SVR), Gaussian process regression (GPR), and decision trees (DTs), have been widely employed in different fields for monitoring and learning tasks [24], [25], [26], [27], [28], [29], [30], [31]. However, despite the numerous applications of AI and ML in RF/microwave engineering, the nonlinear region associated with cavity perturbation has not been thoroughly investigated. Recently, an ML-based approach was proposed to tackle the nonlinearity challenges present in cavity perturbation, but its application remains limited to estimating dielectric constants [31].

Keeping an eye on the above issues, this article utilizes the capabilities of the DT and ensemble learning (EL) methods to expand cavity perturbation methods and make

Received 14 April 2025; accepted 24 May 2025. Date of publication 30 May 2025; date of current version 25 July 2025. This work was supported in part by the Nazarbayev University Collaborative Research Program (CRP) under Grant 111024CRP2018, and in part by the Nazarbayev University Faculty Development Research Grant (FDRG) under Grant 201223FD2601. *(Corresponding author: Mohammad S. Hashmi.)*

Ahmad Khusro and Mohammad S. Hashmi are with the Department of Electrical and Computer Engineering, School of Engineering and Digital Sciences, Nazarbayev University, Astana 000010, Kazakhstan (e-mail: ahmad.khusro@nu.edu.kz; mohammad.hashmi@nu.edu.kz).

Zubair Akhter is with IMPACT LAB, CEMSE Division, King Abdullah University of Science and Technology, Jeddah 23955, Saudi Arabia, and also with the Directed Energy Research Center, Technology Innovation Institute, Abu Dhabi, UAE (e-mail: zubair.akhter@kaust.edu.sa).

Abhishek K. Jha is with the Department of Electrical Engineering, Indian Institute of Technology Tirupati, Tirupati 517506, India (e-mail: akj@iittp.ac.in).

Atif Shamim is with IMPACT LAB, CEMSE Division, King Abdullah University of Science and Technology, Jeddah 23955, Saudi Arabia (e-mail: atif.shamim@kaust.edu.sa).

Digital Object Identifier 10.1109/JIOT.2025.3575287

complex permittivity extraction possible in the nonlinear region. In addition to this, the proposed sensing node (i.e., the cavity resonator) has been successfully integrated with an IoT framework for wider applicability by enabling material measurement remotely. Overall, the main contributions of this article are as follows.

1) Development of a compact and robust novel regression trees-based model with minimum modeling parameters for complete characterization of dielectric samples in the nonlinear region of cavity perturbation.
2) Excellent retrieval accuracy testing samples with extrapolated thicknesses demonstrating the scaling capability of the trained ML model;
3) Rapid learning capacity, adaptation capability, and ability to model nonlinearity.

The remainder of this article is organized as follows. Section II details the IoT-based sensing architecture, including the design of the sensing node with comprehensive numerical simulation results and challenges that justify the need for an innovative proposed regression tree model, and the networking layer, which is crucial for data acquisition and transfer to the cloud. Section III focuses on the development of regression tree-based models, outlining the theoretical and algorithmic frameworks for the DT and the EL, as well as the training, testing, and validation processes for these models. Section IV examines the application layer of the proposed IoT-based microwave dielectric material characterization (MDMC) system. Finally, Section V provides the concluding remarks.

II. IoT Sensing Architecture for MDMC

A. Overview of IoT Framework

Fig. 1 presents the overarching architecture of a four-layer IoT-based smart system for MDMC. These layers are organized from bottom to top as the sensing layer, network layer, data processing layer, and application layer. Unlike other IoT frameworks, a service-oriented architecture (SOA) is employed because of its robust integration of the network and data processing layers, ensuring smooth and efficient operation. The key features of SOA—modularity, interoperability, scalability, reusability, and flexibility—contribute to a structured and efficient management of the complexities inherent in IoT systems. This ultimately leads to smoother operations compared to other architectural approaches that may not offer the same level of adaptability and integration.

Fig. 2 depicts the proposed SOA structure, organized into four interconnected layers that illustrate the data flow from sensors to end-user devices. The first, i.e., the sensing layer, utilizes the TM_{111} mode of the circular cavity sensor for the precise characterization of dielectric materials. The sensing nodes, connected to the measuring unit [a vector network analyzer (VNA)], can be geographically distributed across multiple locations. The network layer is responsible for data transmission, where wireless communication protocols are used to transmit data from the sensing nodes to the next stage. The gateway acts as the central hub in this layer, collecting data from the sensing nodes via Bluetooth and transmitting it to the Data Processing Layer via Ethernet.

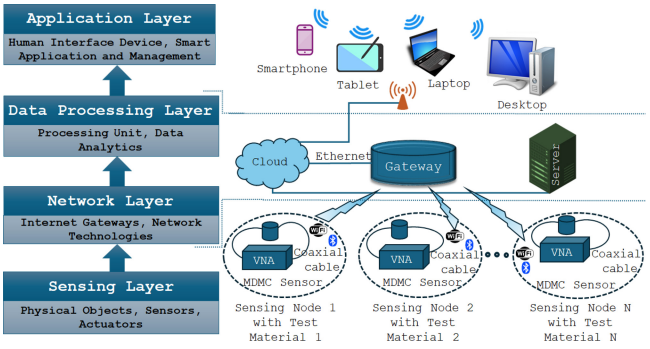

Fig. 1. Schematic representation detailing the integration and interaction of entities within an IoT-based MDMC system for industrial applications.

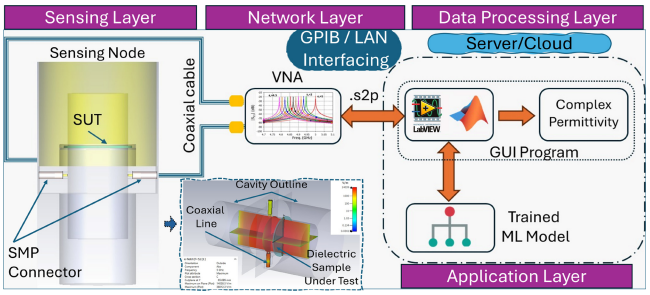

Fig. 2. Schematic representation of interconnected layers in SOA-based MDMC system for industrial monitoring and processing (sensing node detailed in scribbled box).

Various communication protocols, such as Wi-Fi and 4G modules, are employed to receive measurement commands and upload S-parameter data to the server via the gateway, depending on the situation and network availability. The third layer, the Data Processing Layer, consists of the processing unit and data analytics components, where a trained ML algorithm is deployed. This algorithm processes the measured S-parameter data from each node to estimate the relative permittivity (ε_r') and the loss tangent ($\tan\delta$). The final layer, the Application Interface Layer, supports user interaction and system integration, displaying the results in a user-friendly GUI. Each of these layers is discussed in detail in the subsequent sections.

B. Implementation of Microwave Sensing Layer

This section provides a comprehensive overview of the sensing methodology employed within the SOA's sensing layer. The proposed sensor is a circular cavity that operates in the TE_{111} mode. Aluminium ($\rho = 3.5 \times 10^7$ S/m at room temperature) is selected as the sensor material due to its advantages in terms of weight, cost, surface treatment, and ease of machining and fabrication compared to copper. The 3-D model of the sensing node, designed to operate at 5 GHz, is depicted in Fig. 3, which provides a comprehensive schematic of the cavity design. Fig. 3(a) depicts the external structure, which features two coaxial SMP-type ports for easy mounting and detachment, streamlining the dielectric testing process. Fig. 3(b) highlights the interior configuration, where the second SMP port is visible on the cavity wall, and the test sample is securely positioned on a custom-designed

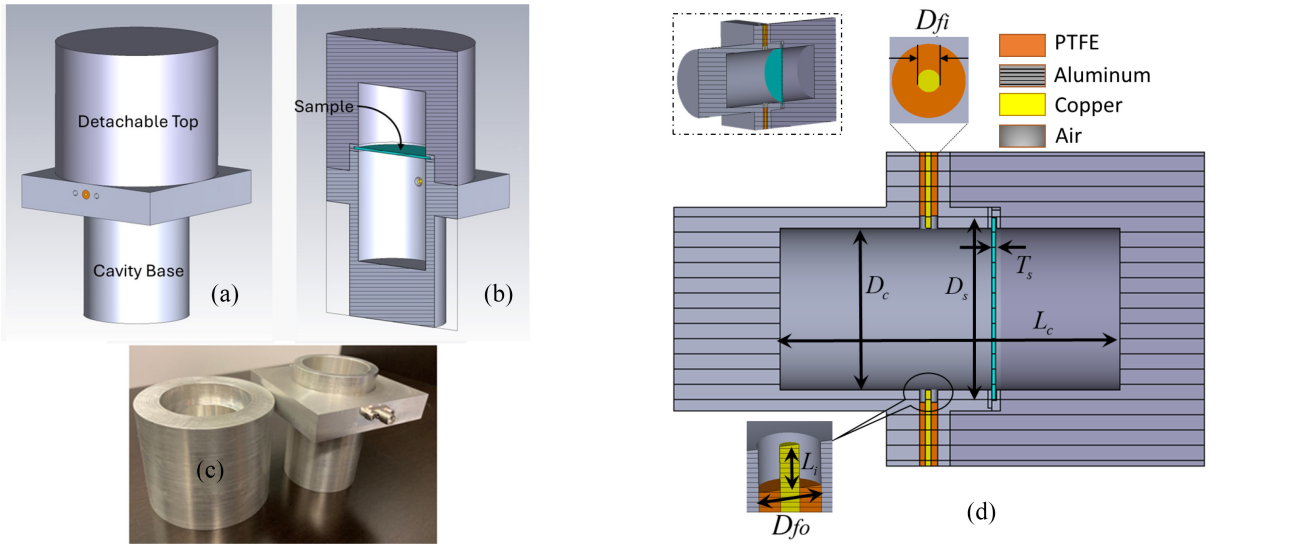

Fig. 3. (a) Exterior and (b) interior cut views of the 3-D electromagnetic model of the proposed cavity, (c) fabricated cavity, and (d) cut / cross sectional view with dimensions.

support platform. Fig. 3(c) presents the fabricated cavity in its open state, ready to accommodate the test sample. Finally, Fig. 3(d) illustrates the various dimensions of the cavity, including an exploded view of finer details for better clarity and understanding. The design parameters are theoretically calculated using the following equation and later fine-tuned in the full-wave electromagnetic simulator

$$(f_r)mnp = \frac{1}{2\pi\sqrt{\epsilon\mu}}\sqrt{\left(\frac{\chi'_{mn}}{a}\right)^2 + \left(\frac{p\pi}{h}\right)^2} \tag{1}$$

where χ'_{mn} represents the nth zero ($n = 1, 2, 3, \ldots$) of the derivative of the Bessel function J_m of the first kind and of order m ($m = 0, 1, 2, 3, \ldots$). The optimized design parameters of the sensing node are listed in Table I. The design of the sensing node prioritizes operation in the TE_{111} mode over the conventional TM_{010} mode, which is achieved by maintaining a height-to-radius $h/a = 4.2$, significantly greater than the critical threshold of 2.03 (for $h/a < 2.03$, TM_{010} is the dominant mode). The TE_{111} mode is preferred for two key reasons: 1) the off-center positioning of the sample within the cavity, as illustrated in Fig. 3(b) and (d), requires a field that is uniform not only along the z-axis but also across the sampl's surface [Fig. 4(a)] and 2) the sample is designed as a thin disc, which improves sensitivity when the electric field is tangential to the disc, as depicted in Fig. 4(b), rather than normal to it, as in the TM_{010} mode. Each cavity design can maintain linearity only up to a certain sample-to-cavity volume ratio, which is directly linked to the cavity's loading. When the loading exceeds a certain threshold, the cavity operation enters the nonlinear region [8]. By enhancing the interaction between the dielectric disc sample and the electric field of the TE_{111} mode compared to the TM_{010} mode, we have maximized the loading for the specified sample thickness. The increased sensitivity of cavity perturbation causes the cavity to enter the nonlinear state much sooner than with the TM_{010} mode. This concept underpins the design of the circular cavity operating in TE_{111} mode, which

TABLE I
CIRCULAR CAVITY DESIGN PARAMETERS

Parameters	D_c	D_s	D_{f_0}	D_{f_i}	L_c	L_i	T_s
Value (mm)	37.90	42.90	4.14	1.27	80	2.92	0.8, 0.9, 1

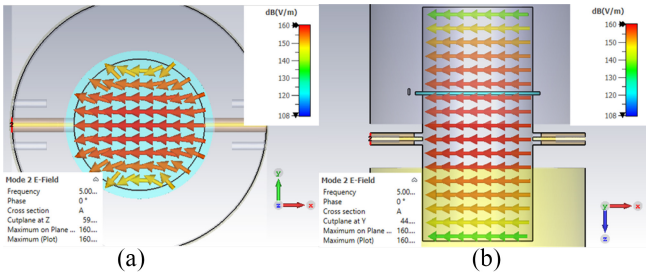

Fig. 4. Arrow type plot of the electric field of (a) TE_{111} mode in XY-plane and (b) TE_{111} mode in XZ-plane, showing the maximum intensity of tangential electric field across the surface of the sample.

rapidly transitions into the nonlinear region, a critical aspect for evaluating the developed AI/ML algorithm. The TM_{010} mode reduces sensitivity due to the weak interaction caused by the sample's small thickness ($\sim$1/60λ). The resonant frequency for the TM_{010} mode is 6.06 GHz, resulting in a frequency separation of more than 1 GHz. The sensing node is fabricated using advanced CNC milling techniques, and its surface finish is achieved through mechanical and chemical polishing, followed by clear anodizing, thus recording a high-quality factor of 9231.

After designing and fabricating the sensing node, which includes a custom-designed support platform to hold the test specimen [as shown in Fig. 3(b)], the disc-shaped sample is positioned at the location of the maximum electric field tangential to its surface to estimate the complex permittivity (as shown in Fig. 4). The real and imaginary parts of the complex permittivity can be determined using the conventional cavity perturbation (CCP) formula, as given in (2) and (3), where Q_0, Q, and f_0, f are the quality factors and resonant

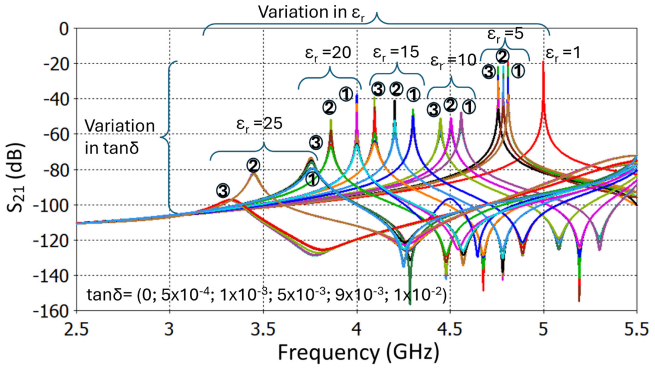

Fig. 5. Simulated transmission response of @1 = 0.8 mm, @2 = 0.9 mm, and @3 = 1 mm thick dielectric disk sample, variation in dielectric constant and loss tangent ranging from 1 to 25 and 0 to 0.01, respectively.

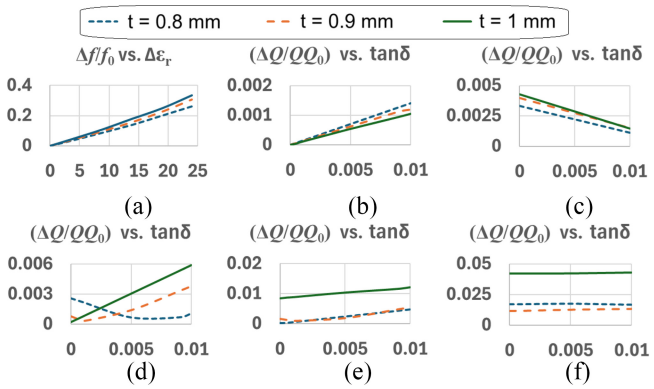

Fig. 6. (a) Change in the fractional resonant frequency vs change in the dielectric permittivity of the test sample, and the change in fractional quality factor to the loss tangent of the test sample for (b) $\varepsilon_r' = 5$, (c) $\varepsilon_r' = 10$, (d) $\varepsilon_r' = 15$, (e) $\varepsilon_r' = 20$ and (f) $\varepsilon_r' = 25$.

frequencies of the unloaded and the loaded cavities, respectively, loss tangent is defined as $(\tan\delta = \varepsilon_r''/\varepsilon_r')$, while A and B are shape factors that depend on the cavity configuration, operating mode, the permittivity and geometry of the sample, as well as the sample's position within the cavity [8]

$$(\varepsilon_r' - 1) = \left(\frac{1}{A}\right)\left(\frac{f_0 - f}{f}\right) \tag{2}$$

$$\varepsilon_r'' = \left(\frac{1}{B}\right)\left(\frac{1}{Q} - \frac{1}{Q_0}\right). \tag{3}$$

The cavity is simulated for three distinct specimens with thicknesses of 0.8, 0.9, and 1 mm using the frequency domain solver of CST Microwave Studio, and the two-port S-parameters are calculated. To ensure a precise measurement of the quality factor, 15 001 frequency points are collected over a frequency range of 2.5 – 5.2 GHz, enabling accurate determination of loss tangent values. The dielectric properties and loss tangent of the test sample were varied to determine the sensitivity of the cavity. A total of 132 samples are generated through simulations for each sample thickness, with ε_r' values ranging from 2 to 25 and six sets of $\tan\delta$ values: [0, 0.0009, 0.0001, 0.006, 0.001, 0.01]. Under no load conditions, the resonant frequency (f_0) and quality factor (Q_0) are determined to be 5 GHz and 9231, respectively, as shown in Fig. 5. The quality factor is calculated using the 3-dB approach. The high value of Q_0 makes the proposed cavity particularly effective for detecting low-loss dielectric samples. Fig. 5 illustrates variations in the cavity transmission coefficient. It was observed that variations in the loss tangent do not influence the frequency response but do modify the insertion loss. Additionally, changes in the dielectric constant not only cause a shift in the frequency response but also result in a significant change in insertion loss, particularly under higher loading conditions.

A detailed study of the dielectric sample with a high dielectric constant reveals that samples with a relative permittivity greater than 10 exhibit significant nonlinear variations in the resonant frequency shift [8]. As shown in Fig. 6(a), a linear relationship is maintained for ε_r' values below 10; however, this linearity breaks down at higher permittivity values. This issue, known as cavity overloading, is a well-known limitation of the CCP method. Furthermore, as the dielectric constant enters the nonlinear region, the assumptions underlying perturbation theory become significantly compromised. The electric field distribution of the TE_{111} mode begins to distort, and nearby modes are also affected. Additionally, it is important to note that further increases in the dielectric constant may push the resonant frequency beyond the cut-off frequency of the circular waveguide. In such cases, the dielectric sample under test interacts primarily with evanescent modes, making it impossible to extract the complex permittivity using (2) and (3). Furthermore, the quality factor of a resonant cavity can increase after introducing an extremely low-loss dielectric, which could invalidate the CCP method, particularly for extremely low-loss dielectric samples [1]. This effect becomes more pronounced when the dielectric material under test has a high dielectric constant. Fig. 6(d)–(f) show that the fractional change in the quality factor is not always uniform with the change in the loss tangent of the test sample, as expected from (3). However, a more linear response is observed for a lower dielectric constant, $\varepsilon_r' = 5$, as shown in Fig. 6(b).

These challenges, such as nonlinear variations in the resonant frequency shift exacerbate the issue of cavity overloading, as previously discussed, and limit the accuracy of MDMC using standard formulae (2) and (3) and serve as the primary motivation to utilize ML techniques for overcoming these issues. The ML-based approach is designed to overcome these challenges in the following ways.

1) ML approach learns complex, nonlinear relationships directly from data, unlike the conventional methods that face issues such as variances in frequency shifts. This allows for more accurate and generalized predictions of material properties.
2) ML model efficiently reduces the impact of perturbation-induced frequency changes by identifying underlying patterns in a massive dataset, which traditional techniques cannot achieve due to severe analytical constraints.
3) Instead of relying simply on established equations, our ML model uses training data from a diverse set of simulations to predict complex permittivity more robustly across a broader range of materials/samples and cavity designs.

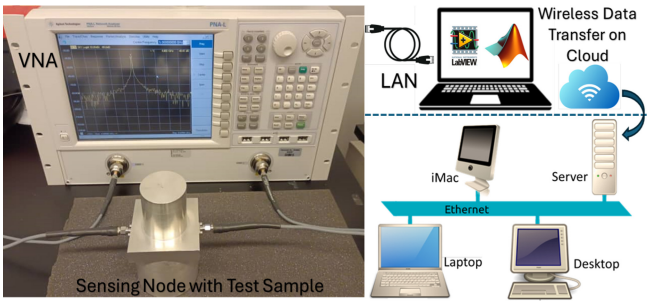

Fig. 7. IoT-based measurement setup depicting sensing node, network, and data processing layers.

4) CCP methods frequently require empirical calibration to account for nonlinearities. In contrast, our ML-based model automates this correction, making the technique more adaptable and requiring less manual intervention.

The proposed ML algorithms used for the present research will be discussed in detail in the data processing section.

C. Network Layer: Measuring and Networking

The networking layer facilitates wireless communication and data acquisition from each sensing node. The measurement setup, which integrates the developed sensing node with a VNA, is depicted in Fig. 7. A two-port calibration over the 2.5–5.5 GHz frequency range is performed using 6401 data points and the short-open-load-through (SOLT) standard to achieve high accuracy. Several communication technologies were evaluated to meet the flexibility and efficient data transfer requirements. Radio-frequency identification (RFID) was found suitable for identification tasks, while ZigBee, despite its energy efficiency, does not meet the necessary data rate requirements. Bluetooth has low power consumption, moderate data rates, and range, but the wireless local area network (WLAN) or Wi-Fi and local area network (LAN) have higher data rates and broader coverage. As illustrated in Fig. 7, the transmission coefficient data for the loaded and unloaded conditions of the sensing node are recorded on a computer connected to the VNA via a LAN network.

The sensing component, VNA, measures the scattering parameters (S-parameters) of a test sample placed between its ports. The parameters S_{11} and S_{21} reflect the electromagnetic interaction with the material under test. The VNA is connected to a host PC (or embedded system) that interfaces the instrument with the data processing environment. The data acquired from the VNA is transmitted to other computational nodes via a LAN. The data is shared over Ethernet or Wi-Fi, depending on the configuration, enabling access by various devices (e.g., desktop, laptop, iMac) locally or remotely. LabVIEW is used for real-time control and communication between the hardware and software layers. It acts as a bridge, facilitating automated data acquisition from the VNA and forwarding it to further processing. The real-time data collected from the VNA is passed to MATLAB, which hosts the proposed ML model. Once the data are received, MATLAB automatically invokes the ML model, processes the input features, and provides the estimated complex permittivity values in real time. The system enables synchronous and automated operation with minimal user intervention. The real-time interaction between LabVIEW and MATLAB ensures low-latency data flow, enabling near-instantaneous material characterization. The integration of cloud services allows for storage and remote monitoring or post-analysis, supporting scalability and collaborative access across locations. The seamless collaboration of sensing hardware, LabVIEW-based control, MATLAB-based analysis, and network communication makes the setup ideal for smart, remote, and scalable sensing applications.

The VNA also supports data transfer through the GPIB interface (IEEE-488), a parallel data transfer protocol, which can be utilized to upload data to a cloud/server for further processing. Once the data are stored in the cloud, processing through the proposed regression tree models for MDMC in the nonlinear region of the sensing node will commence, as discussed in the following section.

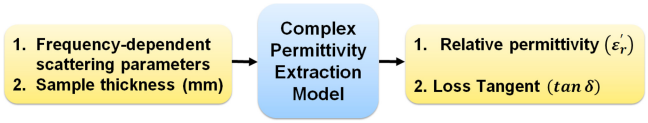

Fig. 8. Generalized ML-based architecture for estimating complex permittivity of dielectric samples.

III. Data Processing Layer: Framework for Model Development

A generalized ML-based model architecture for estimating complex permittivity is illustrated in Fig. 8. The model maps seven predictors: 1) quality factor (Q_f); 2) 3-dB bandwidth (BW); 3) resonant frequency (f_r); 4) measured frequency (f_m); 5) sample thickness (t); 6) transmission coefficient magnitude $|S_{21}|$ and reflection coefficient magnitude $|S_{11}|$ to the feature space to predict relative permittivity (ε_r'); and 7) the loss tangent ($\tan\delta$) of the dielectric samples. In this research, we have preferred nonparametric ML techniques, such as DT and EL to train/develop the regression models and retrieve the complex permittivity of dielectric materials in linear and nonlinear regions. These nonparametric models offer several advantages: reduced computational time and space complexity, straightforward interpretability, robustness to missing features, and minimal feature processing requirements [32], [33], [34], [35], [36], [37], [38]. The compelling reasons for choosing nonparametric models DT and EL over other popular techniques, such as neural networks (NNs) or support vector machines (SVMs), to handle regression problems in ML are further discussed.

With a large number of predictor variables, any tree-based model will perform slightly better. The reason is that the DT can create several thousand trees with a higher depth level, thereby almost learning all of the training space with all possible combinations. A tree cuts and divides the feature space recursively to get an informative separation [32], [33]. In such circumstances, we require additional data to build a better model, which is supported by our approach and the quantity of the dataset. NNs have different methods for utilizing the input space, which depend on the initialization of the weights and bias. Random initialization of weights and bias, where weights and bias are fixed between [–1,

1], neurons have a higher probability of lying outside the input space. The unused training space may lead to poor training [39]. We require a large data set to improve the model's performance during training. On the other hand, the SVM divides the feature space once, based on parameters for all points, learned via an objective function [26]. Due to data limitations, SVM may struggle to find meaningful patterns to train the data effectively. Therefore, it can be concluded that since these techniques do not utilize the feature space completely and are data dependent, they are not as versatile as tree-based approaches.

In essence, we are searching for a hypothesis space to determine which model best fits our data when we train a single model, such as a DT, SVM, or NN. It can be difficult to find the perfect hypothesis due to data, algorithms, or processing resource limits. This issue is addressed by EL, which integrates the output of several models that should, in principle, function better [33], [34], [35], [36], [37], [38]. The goal is to use the strengths of each model in combination to surpass any one model in terms of prediction. It is possible that each model performs better in some areas of the problem or makes various kinds of errors. EL frequently uses multiple models in parallel, through methods such as voting or averaging, with substantial variation to minimize these errors and generate a final model with high prediction accuracy by lowering the final model's sensitivity to errors and outliers and reducing variance. DT and EL have fewer hyperparameters (1 and 4, respectively) compared to SVMs and neural networks, which makes them optimize in a quick time. The advantages of nonparametric techniques like DT and EL over NNs and SVMs are briefly summarized in Table II.

The following subsections entail the theoretical framework of the regression tree models applied in this study, such as DT and EL, along with their respective algorithms employed for the training/development of the model. Further, the sections will also cover model testing and validation. A comparative analysis of the DT and EL models will also be presented, focusing on the model parameters, architecture, and performance across the training set, test set, and extrapolation range.

TABLE II
KEY ADVANTAGES OF DT AND EL IN PREDICTIVE MODELING: REASONS FOR PREFERENCE

Decision Tree (DT) [32] - [33]	**Ensemble Learning (EL)** [33] - [38]
Handling Nonlinear Relationships: DTs are adept at capturing nonlinear relationships by recursively partitioning the data. While NNs and SVMs can model nonlinear patterns, they require large amounts of data and careful tuning.	**Enhanced Generalization Performance:** EL combines multiple models to improve predictive accuracy and robustness by aggregating diverse models, reducing overfitting, and enhancing performance on unseen data.
Computational Efficiency: DTs are computationally less expensive than NNs and SVMs, requiring fewer resources for training and inference, making them more scalable.	**Reducing the Risk of Overfitting:** EL methods such as bagging and boosting reduce overfitting by averaging out biases and variances across multiple models, making predictions more stable and reliable.
Minimal Data Preprocessing: DTs handle both numerical and categorical data without extensive preprocessing such as normalization or one-hot encoding, simplifying the data preparation process.	**Handling Complex Data Distributions:** EL methods integrate the strengths of multiple base learners, allowing them to model intricate relationships in data more effectively than standalone models like NNs and SVMs.
Robustness to Irrelevant Features: DTs inherently perform feature selection by identifying the most informative features for splitting, making them resilient to redundant or irrelevant features. In contrast, NNs and SVMs may be more sensitive to irrelevant features, potentially impacting their performance.	**Computational Efficiency:** Training multiple simple models in an ensemble can be more computationally efficient than training a single complex NN. Parallelization of EL models further reduces training time and computational costs.
	Flexibility and Versatility: EL allows combinations of different model types, making them adaptable to various problem domains. This flexibility contrasts with the rigid structures of NNs and SVMs, which may require extensive tuning.

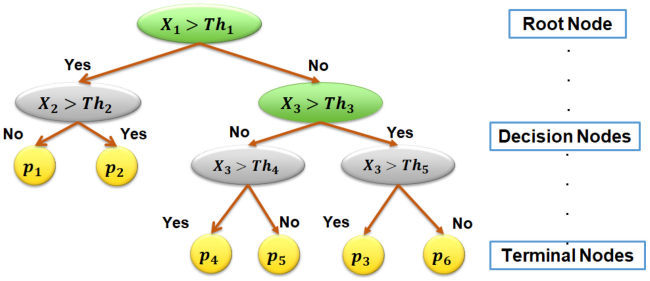

Fig. 9. Basic illustration of DT for regression problems.

A. Decision Tree: Basic Theory and Training Algorithm

DT is a nonparametric ML technique with a tree structure. It consists of the root, decision, and leaf nodes. The root node of a DT leads to a series of decision nodes that represent the individual decisions to be made. The leaf nodes extend from the decision nodes and represent the outcome of those decisions. Each decision node represents a split point, and the leaf nodes that arise from it define the possible outcomes [32]. The illustration of the working of DT is shown in Fig. 9. Let us assume that the input characteristics are represented by $X = \{X_1, X_2, \ldots, X_k\}$. The threshold values used for comparison are represented by $Th = \{Th_1, Th_2, Th_3, \ldots, Th_k\}$, whereas the predicted values are represented by $P = \{p_1, p_2, p_3, \ldots, p_k\}$.

Consider $y \in R$ for the complex permittivity and $X \in S \subset R^s$ for the input features used to predict the complex permittivity, where s is the number of input features in the feature space S. Let $(X_i, y_i)_{i=1}^n$ be the data that will be trained with a DT algorithm. The DT approach recursively divides the feature space S into l leaves: $S_1, S_2, \ldots, S_l$ (subpartitions), indicating distinct divisions without overlap and minimizing an objective function, viz. mean-squared error (MSE). The training course entails the following steps: choosing the optimal tree (minimum leaf size), choosing splits, deciding when to

Algorithm 1 DT Algorithm

Input: Training dataset: $(X_1, y_1), (X_2, y_2), ..., (X_N, y_N)$ consisting of N training samples with m features.
Modeling parameter (variable): Minimum Leaf Size (Search Range: 1-3060204)
Steps
1) Construct Tree: Split the data recursively based on features until stopping criteria are met.
Initialize depth: $d \leftarrow 0$ ▷ Initialize depth of the tree
Initialize stopping flag: $endtree \leftarrow 0$ ▷ Flag to indicate when to stop
Initialize tree nodes: $Node(0) \leftarrow 1$, $Node(1) \leftarrow 0$, $Node(2) \leftarrow 0$ ▷ Initialize tree nodes
while $endtree < 1$ **do** ▷ Continue until stopping condition is met
  if $Node(2^d - 1) + Node(2^d) + \cdots + Node(2^{d+1} - 2) = 2 - 2^{d+1}$ **then**
    $endtree \leftarrow 1$ ▷ Stopping condition met
  else
    for $i \leftarrow 2^d - 1$ to $2^{d+1} - 2$ **do** ▷ Iterate over nodes at current depth
      if $Node(i) > -1$ **then** ▷ If node exists, perform split
        Split tree ▷ Divide current node into child nodes
        $Node(2i + 1) \leftarrow -1$ ▷ Mark left child as unavailable
        $Node(2i + 2) \leftarrow -1$ ▷ Mark right child as unavailable
      end if
    end for
  end if
  $d \leftarrow d + 1$ ▷ Move to the next depth level
end while
2) Termination Criteria:
i **If** mean-squared error (MSE) = 1e-5, **then** stop
ii **If** No. of Iterations = 30, **then** stop
3) Prediction: Return the average of target values at a specific leaf node in the tree.
Return the calculated prediction, $\hat{y}_{test}$
Output: Return $\hat{y}_{test}$ for the test set of inputs.

terminate splitting, and deciding on prediction accuracy criteria [32]. Algorithm 1 provides the pseudocode for developing a compact DT-based complex permittivity extraction model. A well-known Bayesian optimization algorithm [39] runs in parallel to obtain an optimal single set of model parameters, i.e., leaf size, that can minimize MSE. During the training course, holdout validation with 25% data is also involved. When using a given tree for prediction, the method sets a weight value w_i for each leaf S_i. If $X \in S_i$, the prediction outcome of an input feature is w_i. The weight w_i is typically defined as the average of the response variable of X that belongs to S_i.

The final step is to determine when to stop splitting, which ultimately depends on obtaining the minimum number of nodes with a maximum iteration set to 30. The final step is to select the right-sized tree, called the optimal tree, which is generally obtained using tree pruning. The tree pruning procedure used in this work is the smallest tree with the minimum error. The proposed DT-based model is less complex and requires less computational burden with a single optimization modeling parameter, i.e., minimum leaf size.

B. Ensemble Methods: Theory and Training Algorithms

EL approaches are broad strategies that combine several good subsets of base models or base learners (BLs) to improve the performance of the ML model and simultaneously accelerate model development. Rather than relying on a single model, a combination rule is used to integrate the predictions made by each learner to produce a more accurate prediction. Weak Learners or BLs are preferred in EL due to several reasons outlined in the following [34], [36], [37], [38].

1) Weak learners (e.g., shallow trees or linear models) accelerate model development compared to full-depth trees or complex NNs because they are computationally light and trained faster. Each weak learner contributes marginally to the ensemble; developers can iteratively refine models in smaller increments, simplifying debugging and tuning processes. Their simplicity helps prevent overfitting to the data in the early stages of the ensemble. In addition, they make ensemble methods more flexible and adaptive by allowing for a gradual correction of errors over multiple iterations.
2) Ensemble methods leverage multiple weak learners to iteratively reduce bias and variance by combining them into strong learners. Each weak learner is trained on the residuals or errors of the previous ones.

In general, EL is divided into two approaches, Bagging and Boosting.

1) Boosted Regression Trees: The Boosted Regression Trees (BSTs) method is a powerful prediction model developed by applying boosting techniques to choice regression/classification tree models. Boosting is a strategy that improves the prediction accuracy of standard regression/classification approaches by combining simple DT models in sequence using BLs.

Boosting can be used for classification or regression problems. In our case, the basic models are regression trees, and the boosting approach is a functional gradient descent [34]. To apply the BST algorithm for predicting complex permittivity, we consider a function $f^*(X)$ such that the error is optimized

$$f^*(X) = \arg\min E(L(y - f(X))) \tag{4}$$

where $L(.)$ is the loss function, which is typically expressed as the squared error loss $L(e) = e^2$, where arg min is the smallest argument that minimizes the error among all feasible functions under consideration. BST employs a summation function in the manner described in the following to approximate $f^*(X)$ [34]

$$f(X) = \sum_{i=1}^{m} f_i(X) \tag{5}$$

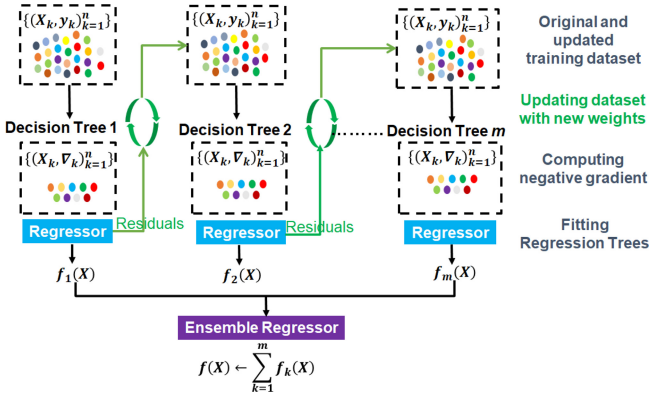

Fig. 10. Schematic representation of the BST Algorithm.

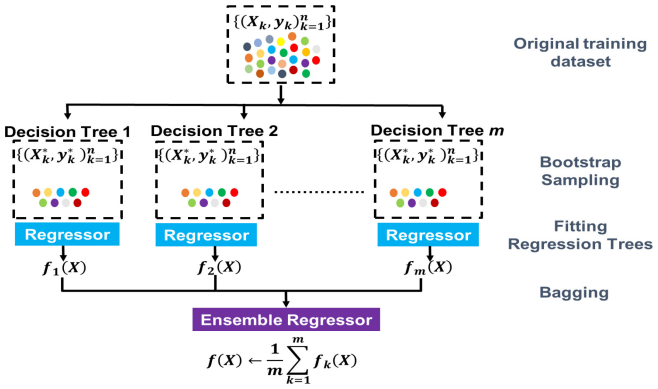

Fig. 11. Schematic representation of BGT Algorithm.

Algorithm 2 BST Algorithm

Input: Training dataset: $(X_i, y_i)_{i=1}^n$, No. of trees = m
A loss function $L(y, f(x))$
Number of Iterations t
Steps
1) Initializing the model with a constant value using $f_0 = \text{argmin}_{\alpha} \sum_{i=1}^{N} L(y_i, \alpha)$
2) **for** $m = 1, 2, ..., K$ **do**
   a) Computing the residuals $r_{mi} = [\frac{\delta L(y_i, f(x))}{\delta f(x)}]_{f(x)=f_{m-1}(x)}$ for $i = 1, 2, .., n$
   b) Started training base learner using the training set $D = x_i$; $r_{mi}{}_{i=1}^{N}$
   c) Obtain ρ_m by using line search optimization $(\rho_m h_m(x)) = \text{argmin}_{\rho,h} \sum_{i=1}^{N} L(y_i, f_{m-1}(x_i) + \rho h(x_i))$
   d) Updating the model: $f_m(x) = f_{m-1}(x) + \rho_m h_m(x)$
end for
Response: Return the final model $f_m(x)$

such that m $f_i(X)$ stands for regression trees. The squared error loss function is commonly used in boosting, where the regression trees are iteratively fitted to the prior fit residuals. The previous errors are gradually reduced by the current fits simultaneously. Furthermore, a small step size is used at each iteration to gradually shift the resultant fit in the function space. The working boosting BST algorithm is summarized using Fig. 10 and Algorithm 2, respectively.

2) Bagging Regression Trees: Bagging regression tree (BGT) is a hybrid algorithm that combines bagging and DTs to improve prediction accuracy. Similarly to the boosting method, it aggregates the output of multiple BLs. The BGT algorithm achieves its performance by generating a predetermined number of DTs (m) and averaging their results. This significantly reduces variation in DTs and tackles the issue of overfitting a single tree in a DT model. Bootstrap sampling is a technique used in BGT to optimize DTs and improve training data. The method includes randomly selecting the original training data set and substituting m uniform samples [34], [35], [37], [38].

To explain the BGT method, consider $(X_i, y_i)_{i=1}^n$ as the complete training data set and m as the number of trees to be formed. During each iteration, a DT is trained with randomly selected bootstrap samples $(X_i, y_i)_{i=1}^n$ from the original training data. Subsequently, a regression tree is iteratively fitted to update the final predictor $f(X)$. Fig. 11 and Algorithm 3 outline the essential processes in computing the BGT algorithm.

Algorithm 3 Bagged Regression Tree Algorithm

Input: Training dataset: $(X_i, y_i)_{i=1}^n$, No. of trees = m
Number of Iterations t
Steps
1) **for** $m = 1, 2, ..., M$ **do**
   i Generate a random bootstrap sample from the training data
   ii Fit a base learner h_j and construct a regression tree $f_i(X)$ using $(X_i, y_i)_{i=1}^n$
end for
Output: Combine the outputs of base learners and update a regression tree $f(X) \leftarrow \frac{1}{m} \sum_{i=1}^{m} f_i(X)$

Using n learners can reduce the prediction variance to $(1/n)$ of that of a single learner. A large number of learners reduces variation and improves prediction performance compared to a small number of learners. To see how the bagging technique minimizes MSE, consider the regression problem with base regressors $b_1(x), b_2(x), \ldots, b_n(x)$.

$$e_i(x) = b_i(x) - y(x); \quad i = 1, 2, \ldots, n \tag{6}$$

$$E_x\Big[(b_i(x) - y(x))^2\Big] = E_x\Big[e_i^2(x)\Big] \tag{7}$$

$$E_1 = \frac{1}{n} E_x\Big[e_i^2(x)\Big]. \tag{8}$$

Assume that an ideal target function of true responses, $y(x)$, is known for a given set of inputs, the distribution $p(x)$ is defined, and the errors are unbiased and uncorrelated, the error for the regression function is calculated using (6)–(11).

$$E_x[e_i(x)] = 0$$
$$E_x\Big[e_i(x)e_j(x)\Big] = 0; i \neq j. \tag{9}$$

Using the average of the individual functions, the regression function is calculated as follows:

$$a(x) = \frac{1}{n} \sum_{i=1}^{N} b_i(x). \tag{10}$$

Therefore, the MSE is given by

$$E_n = E_x\left[\frac{1}{n}\sum_{i=1}^{N} b_i(x) - y(x)\right]^2 = E_x\left[\frac{1}{n}\sum_{i=1}^{N} e_i\right]^2$$
$$= \frac{1}{n^2}E(x)\left[\sum_{i=1}^{N} e_i^2(x) + \sum_{i\neq j} e_i(x)e_j(x)\right] = \frac{1}{n}E_1. \quad (11)$$

It has been demonstrated above that we can decrease the mean squared error by a factor of n by averaging the individual responses. The primary feature of bagging is its ability to drastically reduce the prediction error variance through model training on various datasets. Because each model is trained using a different set of training data, and its prediction errors significantly decrease over the averaging phase, bagging thus offers a considerable advantage. Furthermore, in certain training datasets, observations from outliers are virtually eliminated. Combining a series of trees in the BGTs model can occasionally make it difficult to understand the generated model. At some cost to interpretability, BGTs improve the quality of prediction results.

The proposed EL-based model utilizes a Bayesian algorithm during training that selects the best model parameters that provide high accuracy and risk of overfitting to avoid separate training in EL-based models. The modeling parameters set along with their search range for EL-based models are the learning rate [0.001, 1], the size of the leaves [1-3060204], the number of BL [10, 500], and the optimal ensemble methods (bagging or boosting).

C. Prediction Results and Discussion

To predict the complex permittivity of dielectric samples in our study, we rely on DT-based and EL-based regression models discussed in the preceding section and compare the performance between these models. Initially, the correlation between the input features X_i and the corresponding responses y_i is investigated in the training data. The training data are built by including $|S_{21}|$, $|S_{11}|$, extracting BW (GHz), Q_f, f_r (GHz) for measured frequency (f_m) range for all cavity samples with thicknesses of 1 mm and 0.8 mm. Hold-out validation (HV) is a popular method for measuring regression prediction error while building proposed regression models. Our study uses 25% HV to generate the proposed models. During training, 25% of the dataset is set aside for testing. This method ensures the reliability of the regression model for handling massive data sets. The cavity with a thickness of 0.9 mm is preserved to test the model. The model was trained according to the DT and EL methods, the optimized set of modeling parameters was obtained, and the performance of the model was evaluated for complex permittivity variables on the train and test sets. To evaluate the performance of the model, we use three metrics: the root mean square error (RMSE), the coefficient of determination R^2, and the mean relative error (MRE). These can be calculated using (12)–(14) [24], [25], [26], [30], [39]

$$\text{RMSE} = \sqrt{\frac{1}{n}\sum_{i=1}^{n}\left(y_i - \widehat{y}_{\text{predict}}\right)^2} \quad (12)$$

TABLE III
OPTIMAL DT-MODEL PARAMETERS AND TRAINING PERFORMANCE

Response/ Parameters	Optimal Leaf Size	MSE	Prediction Speed (obs/sec)	Training Time (secs.)	R^2
ε_r'	4644	$3.03\text{x}10^{-4}$	$3.8\text{x}10^{6}$	421.69	1
$\tan\delta$	1285	$4.1\text{x}10^{-11}$	$2.6\text{x}10^{6}$	419	1

TABLE IV
OPTIMAL EL-MODEL PARAMETERS AND TRAINING PERFORMANCE

Response/ Parameters	EL Method	No. of BL	Leaf Size	Learn Rate	MSE	Train. Time	R^2
ε_r'	BGT	28	50	-	$7.63\text{x}10^{-4}$	11019	1
$\tan\delta$	BST	204	2062	0.53911	$4.13\text{x}10^{-11}$	11038	1

$$R^2 = 1 - \frac{(y_i - y_{\text{mean}})^2}{\left(y_i - \widehat{y}_{\text{predict}}\right)^2} \quad (13)$$

$$\text{MRE}(\%) = \left|\frac{y_i - \widehat{y}_{\text{predict}}}{y_i}\right| * 100 \quad (14)$$

where y_{mean} is the mean response value and $\widehat{y}_{\text{pred}}$ is the predicted value. The optimal model parameters and model performance on the training set for both the DT and EL-based models are shown in Tables III and IV, respectively. The DT-based model is relatively more compact with only one model parameter, i.e., leaf size (no. of leaves involved in building a DT model). The optimal leaf size obtained for a trained DT-based model to extract ε_r' and $\tan\delta$ is 4644 and 1285, respectively. In contrast, BL (number of trees) involved in the building of the EL-based model for the extraction of ε_r' and $\tan\delta$ are 28 and 204, respectively, with a leaf size of 50 and 2062. The number of BLs in the EL model indicates the number of trees involved in developing a bagged regressor, as illustrated in Fig. 11. BLs help speed up model development. Furthermore, since the EL-based model is created using a large number of DTs with different leaf sizes, it is evident that the DT-based model is trained more quickly. In addition, four variables are required, as opposed to just one in the case of DT, to maximize the model's performance.

Table V presents a comparative analysis of the two models developed for accurate retrieval of the complex permittivity of dielectric samples on the train set for various sets of inputs, such as Q_f, f_r, and 3-dB BW. The table includes the prediction on diverse dielectric samples with $\varepsilon_r' = 2$ to $\varepsilon_r' = 25$ regions with low values of $\tan\delta$. It is evident from Table V and Fig. 12 that the DT-based model shows slightly better or approximate accuracy for predicting ε_r' than EL-based models on train sets both in the linear and nonlinear regions with MRE as high as 2.8% and 1.6% for sample thicknesses of 1 and 0.8 mm, respectively. However, the EL-based model performs better than the DT-based model in predicting $\tan\delta$ on training sets with MRE as high as 4.2% and 8% for sample thicknesses of 1 and 0.8 mm, respectively. The exact prediction with 0% error can be seen in the DT-based model very frequently, as the DT algorithm works on the principle of splitting a node into child nodes.

The section further investigates the interpolation accuracy of the DT and EL-based models by testing on a circular cavity designed with a thickness of 0.9 mm with a similar

TABLE V
MODEL VALIDATION ON TRAIN SETS WITH THE SAMPLES OF THICKNESSES 1 mm AND 0.8 mm

Parameter/ Samples	f_r (GHz)	Q_f	BW (GHz)	Thickness (mm)	ε_r' (Actual)	$\tan\delta$ (Actual)	ε_r' (Predicted-DT)	$\tan\delta$ (Predicted-DT)	ε_r' (Predicted-EL)	$\tan\delta$ (Predicted-EL)
Sample 43	4.688	10765.785	$4.35475\text{x}10^{-4}$	1	6	0	6	0	5.96363	$9.53\text{x}10^{-6}$
Sample 51	4.618	3533.609	$1.307\text{x}10^{-3}$	1	7	0.0009	7	0.0009	7	0.00090003
Sample 56	4.547	7902.394	$5.75447\text{x}10^{-4}$	1	8	0.0001	8	0.0001	8	0.0001
Sample 64	4.477	558.038	$8.022\text{x}10^{-3}$	1	9	0.006	9	0.006	9.0818	0.006269
Sample 71	4.406	2456.508	$1.794\text{x}10^{-3}$	1	10	0.001	10	0.0009	10.1145	0.0009696
Sample 105	4.011	1897.983	$2.113\text{x}10^{-3}$	1	16	0.0009	16	0.0009	16	0.00090095
Sample 109	3.951	12047.776	$3.27972\text{x}10^{-4}$	1	17	0	17	0	17	$2.14\text{x}10^{-8}$
Sample 116	3.894	7184.881	$5.41914\text{x}10^{-4}$	1	18	0.0001	18	0.0001	17.9092	0.00010226
Sample 126	3.784	179.303	0.0211	1	20	0.01	20	0.01	19.9545	0.009976
Sample 130	2.509	147.389	0.01702	1	25	0.006	25	0.006	25	0.00600042
Sample 265	4.961	8638.132	$5.74337\text{x}10^{-4}$	0.8	2	0	2.031568	0	2.0239606	$3.21\text{x}10^{-8}$
Sample 281	4.915	5740.037	$8.56264\text{x}10^{-4}$	0.8	3	0.001	3	0.00089	3.06301	0.00097964
Sample 285	4.891	5539.537	$8.829006\text{x}10^{-4}$	0.8	3.5	0.0009	3.5	0.0009	3.45948	0.00089908
Sample 294	4.866	1070.579	$4.545\text{x}10^{-3}$	0.8	4	0.01	4	0.01	3.9529	0.0097564
Sample 302	4.815	7403.12	$6.503866\text{x}10^{-4}$	0.8	5	0.0001	5	0.0001	4.9587	0.00010577
Sample 340	4.48	558.062	$8.029\text{x}10^{-3}$	0.8	11	0.006	11	0.006	11.12272	0.00623
Sample 343	4.422	7855.709	$5.607779\text{x}10^{-4}$	0.8	12	0	12	0	12	$1.16\text{x}10^{-8}$
Sample 353	4.366	2230.433	$1.957\text{x}10^{-3}$	0.8	13	0.001	13	0.0009	12.9281	0.00104
Sample 357	4.311	2266.143	$1.902\text{x}10^{-3}$	0.8	14	0.0009	14	0.0009	13.9545	0.000937
Sample 366	4.256	256.319	0.0166	0.8	15	0.01	15	0.01	15	0.010000278

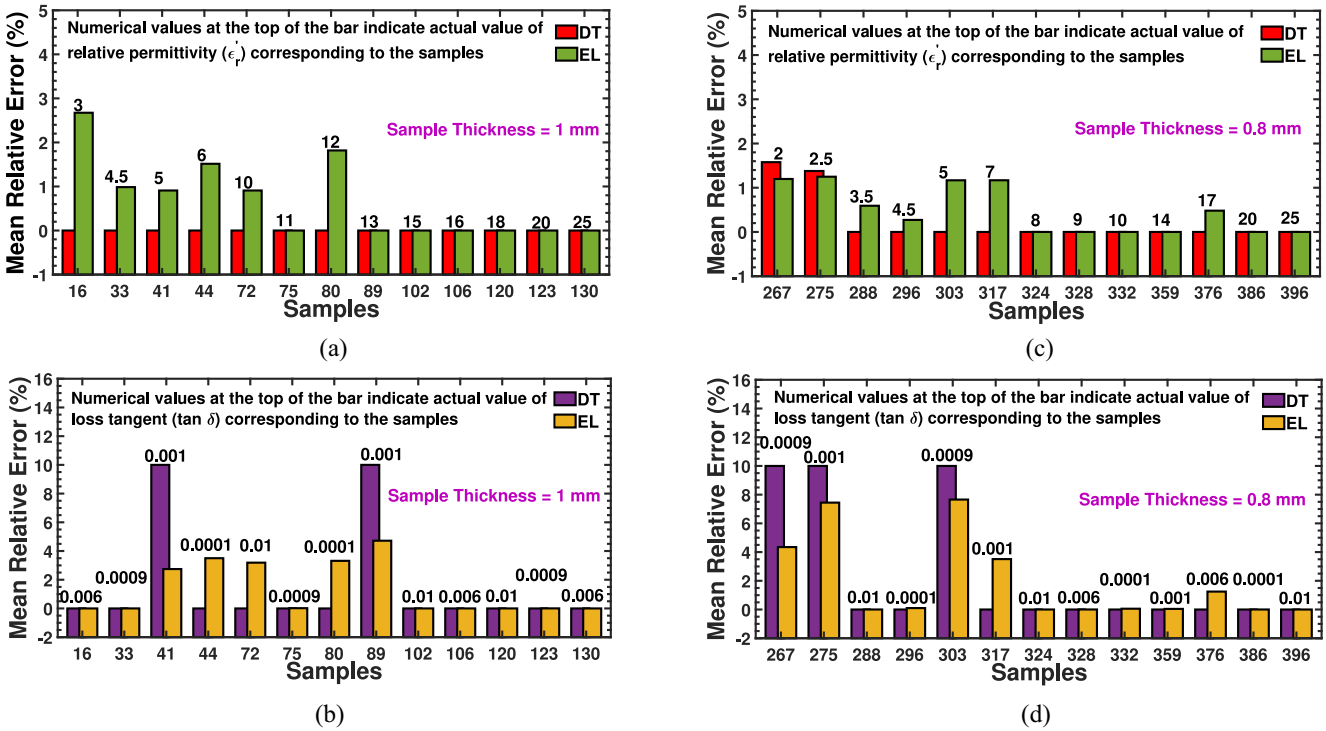

Fig. 12. Comparative analysis between DT-based model and EL-based model in terms of MRE for (a) ε_r' for the thickness of 1 mm, (b) $\tan\delta$ for the thickness of 1 mm, (c) ε_r' for the thickness of 0.8 mm, and (d) $\tan\delta$ for the thickness of 0.8 mm.

set of inputs, such as Q_f, f_r, and 3-dB BW. A comparative analysis of the prediction results for the 0.9 mm cavity is shown in Table VI for various dielectric samples. A similar pattern of the train set is also observed in the test set. This indicates the absence of issues, such as underfitting or overfitting of the proposed DT- and EL-based models, which is critical in ensuring highly accurate ML models. The DT-based model shows higher precision than the EL-based model in predicting ε_r' ranging from 2 to 25 with maximum MRE reaching 1.8%. In the case of predicting $\tan\delta$, the EL-based model outperforms the DT-based model with the highest recorded MRE of 9% compared to 12% for the DT-based model, as evident in Fig. 13 and Table VI.

It is apparent from the above results and discussion that the DT model performs better than the EL model to retrieve ε_r'. This can be understood by analyzing the key hyperparameter differences in Tables III and IV, respectively, i.e., leaf size in DT (4644) versus leaf size (50) and number of BLs (28) in EL. A larger leaf size indicates that the DT model is more generalized and does not overfit to minor variations in the training data. A leaf size of 4644 also suggests that each terminal node (leaf) contains a relatively large number of training samples, making the tree less sensitive to noise and outliers in the dataset. This results in a more stable model with lower variance and better generalization to predict ε_r', which may have a smoother dependency on the input features.

TABLE VI
COMPARATIVE ANALYSIS BETWEEN DT-BASED AND EL-BASED MODELS ON TEST SETS WITH THE SAMPLE THICKNESS OF 0.9 mm

Parameter/ Samples	f_r (GHz)	Q_f	BW (GHz)	ε_r' (Actual)	$\tan\delta$ (Actual)	ε_r' (Predicted-DT)	$\tan\delta$ (Predicted-DT)	ε_r' (Predicted-EL)	$\tan\delta$ (Predicted-EL)
Sample 133	4.959	6267.734	$7.91132\text{x}10^{-4}$	2	0	2.031569	0.0001	2.123925	$5.54175\text{x}10^{-6}$
Sample 149	4.906	4312.805	$1.138\text{x}10^{-3}$	3	0.001	3	0.001	3.04784	0.00100011
Sample 153	4.879	4151.274	$1.175\text{x}10^{-3}$	3.5	0.0009	3.5	0.0009	3.494997	0.00090013
Sample 166	4.822	1210.211	$3.985\text{x}10^{-3}$	4.5	0.006	4.5	0.0066	4.5736301	0.0063
Sample 171	4.793	3453.993	$1.388\text{x}10^{-3}$	5	0.0009	5	0.0009	4.92911	0.00089991
Sample 176	4.733	5025.244	$9.417492\text{x}10^{-4}$	6	0.0001	6	0.0001	6	0.0001
Sample 186	4.671	485.481	$9.62\text{x}10^{-3}$	7	0.01	7	0.01	7	0.0099965
Sample 191	4.608	2412.448	$1.91\text{x}10^{-3}$	8	0.001	8	0.00097	8	0.00092
Sample 193	4.544	5035.835	$9.02343\text{x}10^{-4}$	9	0	9	0	9	$6.55\text{x}10^{-8}$
Sample 202	4.477	535.017	$8.367\text{x}10^{-3}$	10	0.006	10	0.006	10.11454	0.00638112
Sample 206	4.414	4748.92	$9.29371\text{x}10^{-4}$	11	0.0001	11	0.0001	11.1036	$9.49687\text{x}10^{-5}$
Sample 222	4.289	260.572	0.01646	13	0.01	13	0.01	13	0.0100013
Sample 225	4.228	2023.629	$2.089\text{x}10^{-3}$	14	0.0009	13.5	0.0009	14	0.00090041
Sample 229	4.168	7088.37	$5.8802\text{x}10^{-4}$	15	0	15	0	15	$1.67\text{x}10^{-7}$
Sample 239	4.11	1718.969	$2.391\text{x}10^{-3}$	16	0.001	16	0.001	16	0.00099976
Sample 244	4.056	340.288	0.01192	17	0.006	17	0.006	17	0.00600018
Sample 254	3.893	5249.604	$7.41647\text{x}10^{-4}$	20	0.0001	20	0.0001	19.9281	$9.43\text{x}10^{-5}$
Sample 264	3.663	181.752	0.02015	25	0.01	25	0.01	25	0.00988183

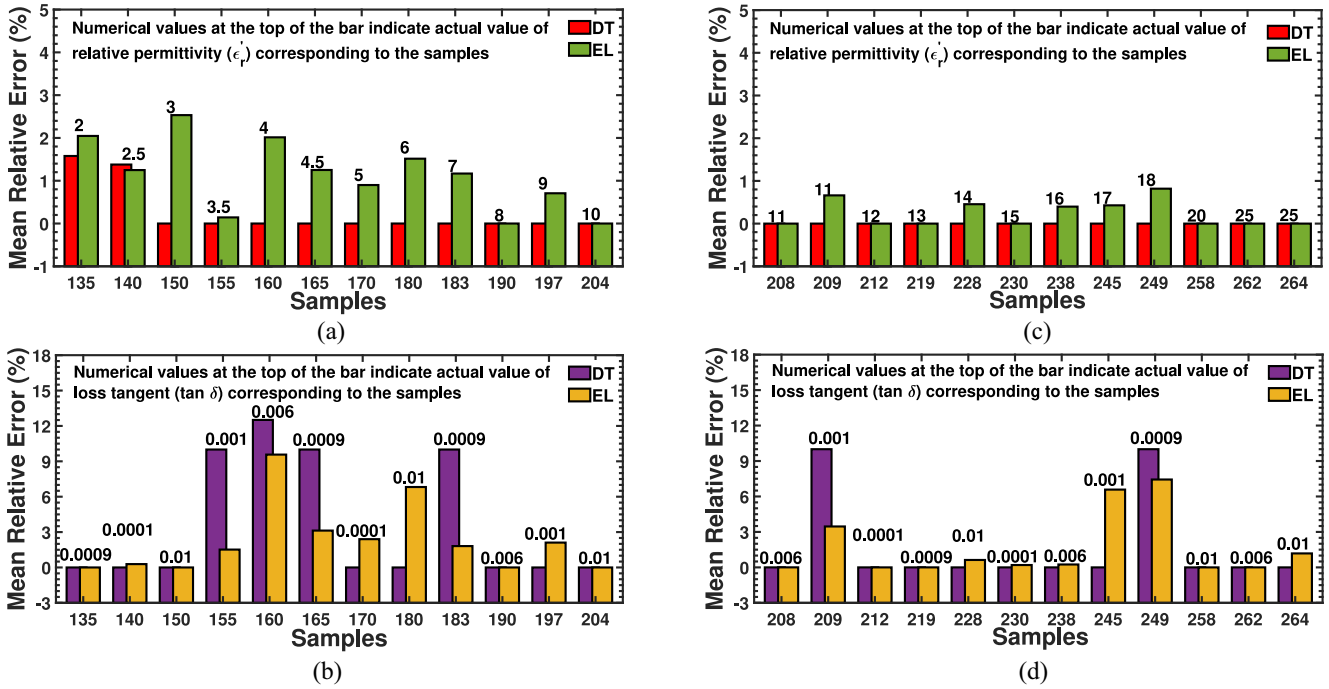

Fig. 13. Comparative analysis between DT-based model and EL-based model in terms of MRE: (a) ϵ_r in the linear region, (b) corresponding tan δ in the linear region, (c) ϵ_r in the nonlinear region, and (d) corresponding tan δ in the nonlinear region. (All results are evaluated for a thickness of 0.9 mm).

For the above-mentioned reason, the DT-based model gives an error of 0% error in predicting ε_r' on a certain number of samples under test as reflected in Tables V and VI, and Figs. 12 and 13. However, in the case of an EL-based model where the BGT algorithm is optimally chosen to extract ε_r, a small leaf size (50) allows individual DTs within the ensemble to capture finer details of the data, but increases variance, making the model more sensitive to noise. Since the BGT algorithm relies on averaging multiple weak learners, each tree must be sufficiently complex to capture complex patterns before averaging stabilizes the predictions. With only 28 BLs, the bagging approach may not be sufficient to fully offset the high variance caused by the small leaf sizes. Bagging works best when the number of weak learners is large (often in the hundreds). With only 28 trees, the ensemble may not achieve its full potential in variance reduction, leading to suboptimal performance compared to a well-tuned single-DT model.

It is the opposite in the case of the models that extract $\tan\delta$ for samples of different thicknesses. It is apparent from Tables III and IV that the leaf size in the case of DT is 1285, and the BLs and leaf size are 204 and 2062, respectively, for the EL model supported by the BST algorithm to predict tan δ. Boosting reduces bias by combining multiple learners. The BST algorithm uses 204 BLs, which means it creates an ensemble of weak models, refining errors at each iteration. Since $\tan\delta$ can exhibit nonlinearity with small and local variations in response to changes in material properties and frequency, iterative refinement of boosting helps to capture

TABLE VII
MODEL VALIDATION FOR NEW SETS OF SAMPLES: MANIFESTING EXTRAPOLATION ACCURACY

Param./ Samples	Thick. (mm)	ε_r' Actual	ε_r' Pred.(DT)	ε_r' Pred.(EL)	ε_r' MRE(%) (DT)	ε_r' MRE(%) (EL)	$\tan\delta$ Actual	$\tan\delta$ Pred.(DT)	$\tan\delta$ Pred.(EL)	$\tan\delta$ MRE(%) (DT)	$\tan\delta$ MRE(%) (EL)
Sample 1 (RO3003)	0.5	3	3.11	3.1019	3.66	3.39	0.001	9.871×10^{-4}	9.89×10^{-4}	1.285	1.035
Sample 2 (RO4003)	0.406	3.38	3.15	3.2244	6.8	4.603	0.0027	0.0025	0.002816	7.4	4.29
Ceramic (C-16, $MgTiO_3$)	1	16	16	15.9592	0	0.255	0.001	0.001	9.812×10^{-4}	0	1.879
Ceramic (C-17, $CaTiO_3$)	1	16	16	16.0909	0	0.568	0.0012	0.00105	0.0011	12.5	8.333
Ceramic (C-5, Al_2O_3)	0.8	10.2	10	9.93	1.96	2.647	0.0012	0.00106	0.00108	11.66	10
Ceramic (C-2, Mg_2SiO_4)	0.8	9.6	9	9.26	6.25	3.541	0.0012	0.001045	0.001073	12.91	10.58
Ceramic (C-9, $MgTiO_3$)	0.8	16	16	15.75	0	1.5625	0.0014	0.00117	0.0016	16.428	12.5

these subtle patterns better than a single DT. The BST-backed EL model has a leaf size of 2062, which means that each terminal node contains a larger subset of training samples compared to DT. This reduces the likelihood of overfitting to noise, which is beneficial for predicting loss tangent, as it often requires smoother approximations rather than overly complex decision boundaries. However, DT might overfit due to its smaller leaf size of 1285 compared to an EL-based model. The DT model has a leaf size of 1285, meaning that it splits more frequently than the EL model. Although this could capture more details, it could also lead to overfitting, making it less generalizable to predict $\tan\delta$, which often follows a smoother trend. The statement and the reason are validated by the results shown in Tables V and VI and in Figs. 12 and 13.

To test the performance of the trained ML model, we validated it with standard ceramic and Rogers laminates used in electronics manufacturing. The proposed ML models were successfully employed to extract the complex permittivity of the various samples. During model testing, we used samples in both interpolation and extrapolation regions compared to the trained data. The interpolation and extrapolation estimations of both models, that is, DT and EL, are summarized in Table VII. It is evident that the trained models provide better accuracy in the interpolation regions and perform well in the extrapolated areas to a certain extent. It is apparent in Table VII that ceramic samples (C-16 and C-9) with similar dielectric constant and loss tangent have differences in errors in the prediction of $\tan\delta$. The main possible reason for the discrepancy is data representation in the proposed ML model. The actual values of the complex permittivity of the C-16 material are ($\varepsilon_r' = 16$, $\tan\delta = 0.001$). The model is trained with a large number of samples with different thicknesses corresponding to the value of C-16. On the other hand, the actual values of the complex permittivity of the C-9 material are ($\varepsilon_r' = 16$, $\tan\delta = 0.0014$). It is important to mention that the trained model does not include any sample observations that include $\tan\delta = 0.0014$. If the training data set contained more instances of materials similar to C-16, the model would have learned a more accurate relationship between the input features and the loss tangent values. The complex permittivity set values of material C-9 belong to a less represented region in the training data, leading to higher generalization errors.

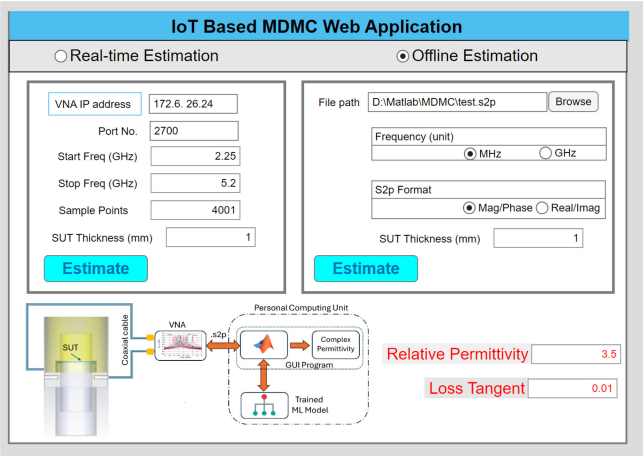

Fig. 14. GUI of the IoT-based MDMC web application.

IV. APPLICATION LAYER

The MATLAB-based application GUI is developed to integrate seamlessly with the trained ML model in the back-end, as illustrated in Fig. 14. This integrated solution estimates the relative permittivity and loss tangent values from the *S*-parameter data measured by the proposed MDMC sensing nodes. The application supports two modes of operation: real-time estimation and offline processing. In real-time mode, the system interfaces with a VNA to capture *S*-parameter data, which is subsequently processed by the pretrained ML model for immediate estimation of material properties. This feature is critical for applications requiring rapid decision-making based on real-time data, offering significant advantages in scenarios where immediate feedback is essential. The offline mode allows for the upload and batch processing of prerecorded *S*-parameter datasets, providing a flexible solution for researchers and engineers who require extensive data analysis without the constraints of real-time equipment operation. This capability is particularly valuable for post-experiment analysis and large-scale data processing tasks. The application GUI facilitates seamless navigation across various measurement nodes using IP address-based identification. The underlying advanced ML algorithms ensure high accuracy in estimating dielectric constants from the measured *S*-parameters. This dual-mode functionality, an intuitive user interface, and precise data processing make the application a powerful tool for

TABLE VIII
COMPREHENSIVE COMPARISON BETWEEN THE ESTABLISHED METHODS AND THE PROPOSED WORK

Features/ Ref.	Technique	Region Covered	Method	Sensing Property	Max. Accuracy (%)		IoT Implementation
					$\varepsilon_r^{'}$	$\tan\delta$	
[8]	Resonant (Rectangular MCP)	Linear and Non-linear	Analytical and Num. Optimization	tan δ and $\varepsilon_r^{'}$	81.03	47.34	No
[9]	Resonant (CSRR)	Linear	Analytical	tan δ and $\varepsilon_r^{'}$	97.28	39.55	No
[10]	Resonant (CCCSRR)	Linear	Analytical	Only $\varepsilon_r^{'}$	91	-	No
[11]	Resonant (Microstrip Line)	Linear	Analytical	tan δ and $\varepsilon_r^{'}$	96.14	50	No
[12]	Resonant (CSRR)	Linear	Analytical	tan δ and $\varepsilon_r^{'}$	98.44	90	No
[13]	Non-resonant (PFSIW)	Linear	Analytical	tan δ and $\varepsilon_r^{'}$	96.67	44.45	No
[14]	Non-resonant (MCCPW)	Linear	Physics Informed ML (ANN)	tan δ and $\varepsilon_r^{'}$	95	90	No
[15]	Non-resonant (GCPW)	Linear	Deep neural network (DNN)	tan δ and $\varepsilon_r^{'}$	98.8	77.2	No
[16]	Non-resonant (Horn-lens antenna)	Linear	Analytical	Only $\varepsilon_r^{'}$	92.91	-	No
[17]	Non-resonant (Coaxial line)	Linear	Analytical	tan δ and $\varepsilon_r^{'}$	96.61	42.11	No
[18]	Non-resonant / free-space (3D printed lens)	Linear	Analytical	tan δ and $\varepsilon_r^{'}$	90	30	No
This work* (Interpolation) (EL)	Resonant (Circular Cavity)	Linear and Non-linear	Physics Informed ML (DT, EL)	tan δ and $\varepsilon_r^{'}$	97.75	90.5	Yes
This work* (Interpolation) (DT)	Resonant (Circular Cavity)	Linear and Non-linear	Physics Informed ML (DT, EL)	tan δ and $\varepsilon_r^{'}$	98.2	87.25	Yes
This work* (Extrapolation) (EL)	Resonant (Circular Cavity)	Linear and Non-linear	Physics Informed ML (DT, EL)	tan δ and $\varepsilon_r^{'}$	95.39	87.5	Yes
This work* (Extrapolation) (DT)	Resonant (Circular Cavity)	Linear and Non-linear	Physics Informed ML (DT, EL)	tan δ and $\varepsilon_r^{'}$	93.2	83.57	Yes

various domains, including materials science, electronics, and quality assurance. The versatility and precision of the IoT-based scheme proposed in MDMC position it as a valuable asset for research and industrial applications.

Finally, Table VIII presents a comparative analysis of different microwave dielectric material characterization techniques, juxtaposing previously established methodologies with the proposed work. The comparison is structured around key attributes, such as technique, region covered, method, sensing property, accuracy, and IoT implementation. The previously established microwave dielectric characterization methods mainly employ resonant or nonresonant techniques, analytical and ML-based approaches, and focus on the extraction of ε_r' and $\tan\delta$ [8], [9], [10], [11], [12], [13], [14], [15], [16], [17], [18]. Resonant techniques reported in [8], [9], [10], [11], and [12] adopted rectangular modified cavity perturbation (MCP), complementary split-ring resonators (CSRR), concentric complementary split-ring resonators (CCCSRR), and microstrip line technology, respectively, and analytical/empirical formulations that predominantly guide these methods. They show a high accuracy for ε_r', reaching up to 98.44%. The precision in retrieving $\tan\delta$ varies significantly, e.g., 50% for microstrip lines and 39.55% for CSRR technology. None of these methods incorporates an IoT-driven implementation. The other established works apply nonresonant techniques with different technologies, such as partially filled substrate-integrated waveguide (PFSIW), modified conductor-backed coplanar waveguide (MCCPW), grounded coplanar waveguide (GCPW), horn-lens antenna, coaxial line, and free-space approach with 3-D printed lens [13], [14], [15], [16], [17], [18]. Some nonresonant approaches integrate ML, e.g., Physics-Informed ANNs together with MCCPW [14] and deep neural networks (DNNs) incorporated with GCPW [15]. The former ML approach incorporating ANN [14] uses two hidden layers and remains accurate with 95% and 90% in extracting ε_r' and $\tan\delta$ respectively, but lacks IoT implementation. The coaxial line technology adopted an analytical framework [17] that

achieves an accuracy of 96.61% and 42.11% to extract the real permittivity and the loss tangent, respectively. The 3-D printed lens approach (free-space) [18] shows the lowest accuracy of 30% for the retrieval of $\tan\delta$, making it less effective for precise dielectric characterization. Most established works lack IoT integration, restricting remote access in real time. The precision in detecting $\tan\delta$ remains relatively low. However, nonresonant methods integrated with ML show a relatively higher accuracy but may require large training data and exhibit higher computational complexity. All reported state-of-the-art works are limited to the characterization of dielectric samples within linear regions.

The proposed work focuses on resonant circular cavity-based sensing. Unlike previous approaches, the proposed model incorporates IoT for remote monitoring and automated data acquisition, which enhances practical usability. This reduces human intervention, making real-time sensing more efficient. The proposed model utilizes regression tree techniques, such as DT and EL. They provide an expedited model training time and are computationally intensive, more interpretable, and work well on moderate to large datasets compared to ANN/DNN, where a massive dataset is required for proper training. The proposed model is evaluated under both interpolation and extrapolation conditions. The proposed method achieves an accuracy of 98.2% (interpolation) and 93.2% (extrapolation) for ε_r', outperforming most existing techniques. The accuracy in retrieval of $\tan\delta$ improves to 97.75% (interpolation) and 95.39% (extrapolation), demonstrating an increased sensitivity in the dielectric characterization of low-loss samples. Unlike previous techniques that mainly cover linear regions, this approach extends to both linear and nonlinear regions, making it more versatile for the characterization of dielectric materials.

V. Conclusion

This article has introduced a novel IoT-based framework that significantly enhances the capabilities of cavity perturbation techniques for extracting complex permittivity in nonlinear regions. The proposed methodology addresses the nonlinearity challenges generally associated with high-dielectric constant materials by integrating a high-performance cylindrical cavity sensor with powerful ML algorithms within an IoT framework. The system, which has used the DT and EL models, has enabled a precise estimation of ε_r' and $\tan\delta$ over a wide range of values. The IoT-based system provides a reliable and complete dielectric material characterization by mapping important input parameters, such as resonant frequency, quality factor, and measured *S*-parameters, into a sophisticated ML framework. The system has offered dual operational modes, real-time and offline, facilitating research and industrial applications with enhanced flexibility and efficiency.

Inevitably, the significance of the present research work extends beyond theoretical contributions; it has substantial practical applications as a proprietary solution in the field. Our work introduces a nonlinear regression model for cavity perturbation and integrates an application layer that enables global access to the solution for users equipped with sensing nodes. This innovative development positions itself as a valuable proprietary resource for research institutions and universities. It empowers these entities to leverage a well-trained ML model to characterize the dielectric samples across both linear and nonlinear regions of cavity perturbation, all of which are accessible through cloud-based technology. This work has advanced the full characterization of dielectric materials by providing a robust and scalable solution that blends the strengths of ML with the flexibility and transformative potential of IoT frameworks, ultimately enhancing the capabilities of researchers and practitioners in dielectric characterization.

Although the proposed method demonstrates promising results for specific solid materials, it is important to acknowledge its current limitations in handling other states of the material, such as liquids and gases. The model's applicability to these types of material may require further investigation, as their distinct properties and experimental challenges, such as appropriate sample holders and state-dependent behavior, can significantly influence model performance. Addressing these aspects in future work will not only broaden the method's applicability but also pave the way for developing specialized ML models tailored to diverse material states.

References

[1] L.-F. Chen, C. K. Ong, C. P. Neo, V. V. Varadan, and V. K. Varadan, *Microwave Electronics: Measurement and Materials Characterization*. Hoboken, NJ, USA: Wiley, 2004.

[2] A. R. von Hippel and S. O. Morgan, "Dielectric materials and applications," *J. Electrochem. Soc.*, vol. 102, no. 3, p. 68C, Mar. 1955.

[3] D. M. Pozar, *Microwave Engineering*. New York, NY, USA: Addison-Wesley, 1990.

[4] J. Krupka, "Frequency domain complex permittivity measurements at microwave frequencies," *Meas. Sci. Technol.*, vol. 17, no. 6, p. R55, 2006.

[5] W. H. Bailey, B. R. Cotts, and P. J. Dopart, "Wireless 5G radiofrequency technology-an overview of small cell exposures, standards and science," *IEEE Access*, vol. 8, pp. 140792–140797, 2020.

[6] J. Pisarov and G. Mester, "The impact of 5G technology on life in 21st century," *IPSI BgD Trans. Adv. Res.*, vol. 16, no. 2, pp. 11–14, 2020.

[7] R. Waldron, "Perturbation theory of resonant cavities," *Proc. IEE C, Monographs*, vol. 107, no. 12, pp. 272–274, 1960.

[8] A. K. Jha and M. J. Akhtar, "A generalized rectangular cavity approach for determination of complex permittivity of materials," *IEEE Trans. Instrum. Meas.*, vol. 63, pp. 2632–2641, Nov. 2014.

[9] F. T. Alharbi, M. Haq, L. Udpa, and Y. Deng, "Characterization of conductor-backed dielectric substrates using a novel resonance-based method," *IEEE Sensors J.*, vol. 22, no. 3, pp. 2099–2109, Feb. 2022.

[10] T. Haq and S. Koziel, "Novel complementary resonator for dielectric characterization of substrates based on permittivity and thickness," *IEEE Sensors J.*, vol. 24, no. 1, pp. 195–203, Jan. 2024.

[11] A. Raveendran and S. Raman, "Complex permittivity extraction of planar dielectrics using a noninvasive microwave transmission line resonant technique," *IEEE Trans. Instrum. Meas.*, vol. 70, pp. 1–8, 2021.

[12] M. Saadat-Safa, V. Nayyeri, M. Khanjarian, M. Soleimani, and O. M. Ramahi, "A CSRR-based sensor for full characterization of magneto-dielectric materials," *IEEE Trans. Microw. Theory Techn.*, vol. 67, no. 2, pp. 806–814, Feb. 2019.

[13] N. K. Tiwari and M. J. Akhtar, "Partially filled substrate integrated waveguide-based microwave technique for broadband dielectric characterization," *IEEE Trans. Instrum. Meas.* , vol. 68, pp. 2907–2915, 2019.

[14] S. Panda, N. K. Tiwari, and M. J. Akhtar, "Computationally intelligent sensor system for microwave characterization of dielectric sheets," *IEEE Sensors J.*, vol. 16, no. 20, pp. 7483–7493, Oct. 2016.

[15] L. Nov, J.-Y. Chung, and J. Park, "Broadband permittivity characterization of a substrate material using deep neural network trained with full-wave simulations," *IEEE Access*, vol. 10, pp. 48464–48471, 2022.

[16] L. Li, H. Hu, P. Tang, R. Li, B. Chen, and Z. He, "Compact dielectric constant characterization of low-loss thin dielectric slabs with microwave reflection measurement," *IEEE Antennas Wireless Propag. Lett.*, vol. 17, no. 4, pp. 575–578, Apr. 2018.
[17] N. K. Tiwari, S. P. Singh, A. K. Jha, and M. J. Akhtar, "Simplified approach for broadband RF testing of low loss magneto-dielectric samples," *IEEE Trans. Instrum. Meas.*, vol. 69, no. 5, pp. 2248–2257, May 2020.
[18] E. Hajisaeid, A. F. Dericioglu, and A. Akyurtlu, "All 3-D printed free-space setup for microwave dielectric characterization of materials," *IEEE Trans. Instrum. Meas.*, vol. 67, pp. 1877–1886, 2018.
[19] A. Nicolson and G. Ross, "Measurement of the intrinsic properties of materials by time-domain techniques," *IEEE Trans. Instrum. Meas.*, vol. 19, pp. 377–382, 1970.
[20] Z. Akhter and M. J. Akhtar, "Free-space time domain position insensitive technique for simultaneous measurement of complex permittivity and thickness of lossy dielectric samples," *IEEE Trans. Instrum. Meas.*, vol. 65, pp. 2394–2405, 2016.
[21] S. C. Mukhopadhyay, S. K. S. Tyagi, N. K. Suryadevara, V. Piuri, F. Scotti, and S. Zeadally, "Artificial intelligence-based sensors for next generation IoT applications: A review," *IEEE Sensors J.*, vol. 21, no. 22, pp. 24920–24932, Nov. 2021.
[22] R. Mittra, R. K. Arya, P. Chaudhary, and A. Nasri, "A novel AI-based antenna design software," in *Proc. IEEE INC-USNC-URSI Radio Sci. Meeting (Joint with AP-S Symp.)*, Florence, Italy, 2024, pp. 213–214.
[23] Y. Sharma, "Machine learning and additive manufacturing based antenna design techniques," Ph.D. dissertation, Dept. Electr. Comput. Eng., Univ. Arizona, Tucson, AZ, USA, 2020.
[24] S. Yang, A. Khusro, W. Li, M. Vaseem, M. Hashmi, and A. Shamim, "Optimization of ANN-based models and its EM co-simulation for printed RF devices," *Int. J. RF Microw. Comput.-Aided Eng.*, vol. 32, no. 3, 2022, Art. no. e23012.
[25] A. Khusro, S. Husain, and M. S. Hashmi, "Combining intelligence with rules for device modeling: Approximating the behavior of AlGaN/GaN HEMTs using a hybrid neural network and fuzzy logic inference system," *IEEE J. Electron Devices Soc.*, vol. 12, pp. 723–737, 2024.
[26] A. Khusro, S. Husain, M. S. Hashmi, A. Q. Ansari, and S. Arzykulov, "A generic and efficient globalized kernel mapping-based small-signal behavioral modeling for GaN HEMT," *IEEE Access*, vol. 8, pp. 195046–195061, 2020.
[27] Q. Wu, H. Wang, and W. Hong, "Multistage collaborative machine learning and its application to antenna modeling and optimization," *IEEE Trans. Antennas Propag.*, vol. 68, no. 5, pp. 3397–3409, May 2020.
[28] R. Zhang, X. Jing, S. Wu, C. Jiang, J. Mu, and F. R. Yu, "Device-free wireless sensing for human detection: The deep learning perspective," *IEEE Internet Things J.*, vol. 8, no. 4, pp. 2517–2539, Feb. 2021.
[29] F. Passos et al., "PACOSYT: A passive component synthesis tool based on machine learning and tailored modeling strategies towards optimal RF and mm-Wave circuit designs," *IEEE J. Microw.*, vol. 3, no. 2, pp. 599–613, Apr. 2023.
[30] S. Husain, M. Hashmi, and F. Ghannouchi, "Comprehensive investigation and comparative analysis of machine learning-based small-signal modelling techniques for GaN HEMTs," *IEEE J. Electron Devices Soc.*, vol. 10, pp. 1015–1032, 2022.
[31] Z. Akhter, A. Shamim, A. Khusro, and A. K. Jha, "Tackling non-linearity in cavity perturbation using machine learning approach," in *Proc. IEEE MTT-S Int. Microw. RF Conf. (IMaRC)*, Kanpur, India, 2021, pp. 1–4.
[32] D. Mienye and N. Jere, "A survey of decision trees: Concepts, algorithms, and applications," *IEEE Access*, vol. 12, pp. 86716–86727, 2024.
[33] Y. Li, X. Wang, J. Pang, and A. Zhu, "Boosted model tree-based behavioral modeling for digital predistortion of RF power amplifiers," *IEEE Trans. Microw. Theory Techn.*, vol. 69, no. 9, pp. 3976–3988, Sep. 2021.
[34] I. D. Mienye and Y. Sun, "A survey of ensemble learning: Concepts, algorithms, applications, and prospects," *IEEE Access*, vol. 10, pp. 99129–99149, 2022.
[35] Y. Bian, Y. Wang, Y. Yao, and H. Chen,"Ensemble pruning based on objection maximization with a general distributed framework," *IEEE Trans. Neural Netw. Learn. Syst.*, vol. 31, no. 9, pp. 3766–3774, 1512, Sep. 2020.
[36] T. Xu, G. Han, X. Qi, J. Du, C. Lin, and L. Shu, "A hybrid machine learning model for demand prediction of edge-computing-based bike-sharing system using Internet of Things," *IEEE Internet Things J.*, vol. 7, no. 8, pp. 7345–7356, Aug. 2020.
[37] Y. Ren, L. Zhang, and P. N. Suganthan, "Ensemble classification and regression—Recent developments, applications and future directions [review article]," *IEEE Comput. Intell. Mag.*, vol. 11, no. 1, pp. 41–53, Feb. 2016.
[38] C. Zhao, R. Peng, and D. Wu, "Bagging and boosting fine-tuning for ensemble learning," *IEEE Trans. Artif. Intell.*, vol. 5, no. 4, pp. 1728–1742, Apr. 2024.
[39] A. Khusro, S. Husain, M. S. Hashmi, and A. Q. Ansari, "Small signal behavioral modeling technique of GaN high electron mobility transistor using artificial neural network: An accurate, fast, and reliable approach," *Int. J. RF Microw. Comp.-Aided Engg.*, vol. 30, no. 4, 2020, Art. no. e22112.

Ahmad Khusro received the B.Tech. degree in electronics and communication engineering from Uttar Pradesh Technical University, Lucknow, India, and the M.Tech. and Ph.D. degrees from Jamia Millia Islamia (A Central University), New Delhi, India, in 2015 and 2021, respectively.

He held a visiting student research position with the King Abdullah University of Science and Technology, Jeddah, Saudi Arabia. He worked as a Postdoctoral Researcher with Nano Lab, Indian Institute of Technology Kanpur, Kanpur, India, and also served as an Assistant Professor with the School of Electronics and Electrical Engineering, Lovely Professional University, Punjab, India. Currently, he is associated with the High-Frequency Measurement and Characterization Laboratory, School of Engineering and Digital Sciences, Nazarbayev University, Astana, Kazakhstan as a Postdoctoral Research Fellow. His research interests include RF/microwave/semiconductor device characterization, modeling and optimization, artificial intelligence / machine learning and its application in RF / microwave electronics, and RF active and passive circuits.

Dr. Khusro also acts as a reviewer for several international journals.

Zubair Akhter (Member, IEEE) received the bachelor's degree in electronics and instrumentation engineering from Anand Engineering College, Agra, India, in 2008, and the M.Tech. degree in RF and microwave engineering from Indian Institute of Technology Roorkee, Roorkee, India, in 2011, and the Ph.D. degree in electrical engineering from the Indian Institute of Technology Kanpur, Kanpur, India, in 2018, with a focus on microwave imaging, sensing, & nondestructive testing of materials, through-wall imaging, and ultrawide-band antennas.

He has recently joined Technology Innovation Institute (TII), Abu Dhabi, UAE, as a Senior Antenna Engineer, and leading a team on antennas and Radome developments. Prior to TII, he was associated with King Abdullah University of Science and Technology, Jeddah, Saudi Arabia as a Postdoctoral Fellow. His ongoing research interests encompass the application of artificial intelligence and machine learning techniques to enhance microwave characterization and develop innovative antenna solutions. His work demonstrates a commitment to advancing the frontiers of knowledge and innovation in engineering, with the goal of making meaningful contributions to both academia and industry. He has authored/co-authored over 68 international publications published in top-notch peer-reviewed journals such as IEEE Transactions on Microwave Theory and Techniques, IEEE Transactions on Antennas and Propagation, IEEE Transactions on Instrumentation and Measurement, IEEE Sensors Journal, and various admired international conferences. He is an inventor of six U.S. patents and has given 23 invited talks at various internationally recognized forums/institutions. His recent contributions include advancements in on-chip antennas, microwave imaging, nondestructive testing for the oil and gas industry, printed flexible electronics, printed transparent antennas, and Chipless RFID-based sensing.

Dr. Akhter is a founding chair of the IEEE Antennas and Propagation Student Branch Chapter (SBC), Indian Institute of Technology Kanpur.

Abhishek K. Jha (Senior Member, IEEE) received the Ph.D. degree in RF and microwave engineering from the Indian Institute of Technology (IIT), Kanpur, India, in 2017.

He held a Postdoctoral position with the Czech Academy of Sciences, Prague, Czechia, and later joined Gdańsk University of Technology, Gdańsk, Poland, as an Assistant Professor with the Department of Microwave and Antenna Engineering in 2018. Since 2021, he has been a faculty member with the Department of Electrical Engineering, IIT, Tirupati, India, where he focuses on RF and microwave technologies. He has authored over 50 publications, holds three patents, and contributed to a book chapter. His research interests include advanced microwave circuits and components, RF sensing, metamaterials, time-varying and applied electromagnetics, and additive manufacturing of RF devices.

Dr. Jha is the recipient of several accolades, including the IEEE MTT-S Microwave Graduate Fellowship in 2015, the Gandhian Young Technological Innovation Award in 2016, and the DST Young Scientist Grant in 2016. He has also been honored with the IDUB Premium Award in Poland, featured as "Alumni in Focus" by IIT Kanpur in 2020, and listed in Stanford University's Top 2% Scientists in 2022. He was awarded consecutive University Gold Medals for securing first rank in the first class of the M. Tech. (Hons.) in 2011 and B.E. (Hons.) in 2009, respectively. He is the founding chair of the IEEE MTT-S Student Branch Chapter at IIT Kanpur. He has delivered plenary talks at international conferences and currently serves as an Associate Editor for the IEEE SENSORS JOURNAL and IEEE ACCESS, alongside actively reviewing for leading journals. In 2023, he received the prestigious Einsteinium Grant from Gdańsk University of Technology.

Atif Shamim (Fellow, IEEE) received the M.S. and Ph.D. degrees in electrical engineering from Carleton University, Ottawa, ON, Canada in 2004 and 2009, respectively.

He was an NSERC Alexander Graham Bell Graduate Scholar with Carleton University from 2007 to 2009 and an NSERC Postdoctoral Fellow with Royal Military College Canada and KAUST in 2009–2010. In August 2010, he joined the Electrical and Computer Engineering Program with KAUST, where he is currently the Chair Professor and Principal Investigator of IMPACT Lab. He was an Invited Researcher with the VTT Micro-Modules Research Center, Oulu, Finland in 2006. He is an author/co-author of one book, three book chapters and close to 400 international publications, an inventor on 40 patents and has given over 120 invited talks at various international forums. His research interests are in innovative antenna designs and their integration strategies with circuits and sensors for flexible and wearable wireless sensing systems through a combination of CMOS and additive manufacturing technologies.

Prof. Shamim and his students have won best paper awards in IEEE ICMAC 2025 and 2021, IEEE IMS 2016, IEEE MECAP 2016, IEEE EuWiT 2008, first prize in IEEE IMS 2019 3MT competition, IEEE AP-S Design Competition 2022 and IEEE MTT-S Design Competition 2024, finalist/honorable mention prizes in IEEE APS 2023, IEEE AP-S Design Competition 2020, IEEE IMS 2017 (3MT competition), IEEE IMS 2014, IEEE APS 2005 and R. W. P. King prize for journal papers in IEEE TAP 2017 and 2020. He has served as the Distinguished Lecturer for IEEE AP-S from 2022 to 2024. He has won the Kings Prize for the best innovation of the year in 2018 for his work on sensors for the oil industry. He was given the Ottawa Centre of Research Innovation (OCRI) Researcher of the Year Award in 2008 in Canada. His work on Wireless Dosimeter won the ITAC SMC Award at Canadian Microelectronics Corporation TEXPO in 2007. He also won numerous business-related awards, including 1st prize in Canada's national business plan competition and was awarded OCRI Entrepreneur of the year award in 2010. He founded the first IEEE AP/MTT chapter in Saudi Arabia in 2013 and served on the editorial board of IEEE TRANSACTIONS ON ANTENNAS AND PROPAGATION from 2013 to 2019, IEEE JOURNAL OF ELECTROMAGNETICS, RF, AND MICROWAVES IN MEDICINE AND BIOLOGY from 2020 to 2024, and as a Guest Editor for IEEE AWPL Special issue in 2019. He is currently the AdCom member for IEEE AP-S, Founding Chair of IEEE AP-S TC-8 (wireless Communication), member of APS Fellow Evaluation Committee, member of APS field awards committee, Chair of APS student travel grants, Vice Chair of IEEE APS MGA Committee and has previously served on IEEE TC on Antenna Measurements (AP-S), Microwave Controls (MTT-S 13), and Additive Manufacturing (CRFID).

Mohammad S. Hashmi (Senior Member, IEEE) received the B.Tech. degree from Aligarh Muslim University, Aligarh, India, the M.S. degree from Darmstadt University of Technology, Darmstadt, Germany, and the Ph.D. degree from Cardiff University, Cardiff, U.K., in 2001, 2004, and 2009 respectively.

He has held research, engineering, and academic positions with the University of Calgary, Calgary, AB, Canada; Cardiff University; Thales Electronics GmbH, Germany; Philips Technology Center, Germany; and IIIT Delhi, India. He is currently an Associate Professor with Nazarbayev University, Astana, Kazakhstan. His research activities have led to one book, three U.S. patents (two pending), and over 300 journals and conference publications. His current research interests include the domain of advanced RF circuits for wireless applications (including wireless power transfer and energy harvesting), emerging RF circuits and applications, AI/ML applications for modeling and optimization of GaN HEMTs, and high- and low-frequency instrumentation.

Dr. Hashmi is an Associate Editor of *IEEE Microwave Magazine*.